INTERNATIONAL JOURNAL OF LATEST TECHNOLOGY IN ENGINEERING, MANAGEMENT & APPLIED SCIENCE (IJLTEMAS)

ISSN 2278-2540 | DOI: 10.51583/IJLTEMAS | Volume XV, Issue VII, July 2026

Multi-Domain Dynamic Simulation and Round-Trip Efficiency Verification of a 90 kW Solar Photovoltaic Adiabatic – Compressed Air Energy Storage (A–CAES) System Using MATLAB/Simscape

P. Matarauka, D. Musademba and C Urayai

Department of Fuels and Energy, Chinhoyi University of Technology, Chinhoyi, Zimbabwe

DOI: https://doi.org/10.51583/IJLTEMAS.2026.150700159

Received: 10 August 2026; Accepted: 15 August 2026; Published: 26 August 2026

ABSTRACT

Adequate electricity is critical enabler for agricultural productivity in Zimbabwe and the Chinhoyi University of Technology (CUT) Farm, which has an aggregate demand of 115.63 kW, is frequently subjected to load shedding due to a structural generation gap of about 700 MW. Solar PV generation has an excellent resource base of 5.5 to 6.5 kWh/m^2/day but has the constraint of not being able to deliver firm and dispatchable generation without a storage system to absorb day time excess and return it as firm and dispatchable generation during the night. In this paper, a multi-domain dynamic model of a 90 kW Solar PV Adiabatic Compressed Air Energy Storage (PV-A-CAES) hybrid system sized with the CUT Farm load profile is developed and verified using the developed dynamic model before the exergy and techno-economic analysis is carried out. The model includes a PV array and incremental-conductance MPPT boost converter, two-loop Field-Oriented Control (FOC) of the machine-side and grid-side boost converter, two-stage intercooled compression and charging train, and a thermal energy storage (TES) that recovers the heat of compression and feeds it back into a radial inflow turbine during discharge. The transient simulation demonstrates that that discharge delivers a steady 90 kW at the design pressure ratio (β = 69.1), and that the discharge-side current and torque responses are well damped. The coordinated gains in compressor, turbine and TES performance increase the simulated RTE from a diabatic operating point at 49.0% to a validated operating point at 132.7 kW and 90 kW, which is checked here against the compressor and turbine performance of the Huntorf plant, as well as against the performance of the McIntosh plant, and carried forward explicitly to the exergy and Levelized-cost analyses that follow this study.

Index Terms: Adiabatic compressed air energy storage, dynamic simulation, exergy analysis, Field-Oriented Control, MATLAB/Simscape, maximum power point tracking, PV-A-CAES, round-trip efficiency, thermal energy storage, transient analysis.

INTRODUCTION

Zimbabwe's electricity sector carries a structural generation deficit of approximately 700 MW [1][2], and the resulting load shedding disrupts irrigation timing, cold storage, dairy milking, and agro-processing at institutions such as the Chinhoyi University of Technology (CUT) Farm, whose own verified aggregate demand has been placed at 115.63 kW, a figure dominated by intermittent, high-inrush equipment, borehole and centre-pivot irrigation pumps, milk-chiller compressors, and seasonal processing loads, that a conventional diesel-backed connection struggles to serve economically. The country receives between 5.5 and 6.5 kWh/m2 per day of solar insolation [3], a resource base strong enough to cover a meaningful share of this demand.

Solar PV generation on its own cannot serve loads that need continuous, reliability-sensitive supply, because its output falls to zero overnight and swings with cloud cover during the day, while irrigation scheduling, cold-chain integrity, and milking-parlor timing on a working farm cannot be rescheduled around the sun. Closing that gap calls for a storage technology able to absorb surplus daytime generation and give it back as firm, dispatchable power in the evening and at night, without introducing a second point of technical or financial fragility into an already resource-constrained system.

ISSN 2278-2540 | DOI: 10.51583/IJLTEMAS | Volume XV, Issue VII, July 2026

Table I positions the candidate storage technologies against the requirements a farm-scale, off-grid-adjacent installation in Zimbabwe imposes: multi-hour duration, tolerance for daily deep cycling, a capital structure that does not depend on imported cell chemistries, and a service life measured in decades rather than in charge cycles. Lithium-ion batteries meet the control and round-trip-efficiency requirements but carry a high capital cost for sustained, multi-hour discharge and a supply chain that is entirely import-dependent for a Zimbabwean buyer [4]. Pumped hydro storage is mechanically mature but requires an elevation difference and a secure water source that a flat farm site does not offer. Flywheels serve power-quality and short-duration ride-through roles well but cannot economically hold multi-hour energy. Hydrogen storage rounds trip at a substantial efficiency penalty and, at farm scale, adds an electrolyzer-storage-fuel-cell chain that is complex to operate and maintain locally [4]. Compressed air energy storage (CAES) is the outlier in this comparison: it scales naturally to the multi-hour, multi-hundred-kilowatt duration and capacity a site like this one needs, it is built from turbomachinery components with a multi-decade service life and an established industrial supply base [5], [6], and, unlike pumped hydro, it does not require a specific topography, only a pressure vessel or a cavern.

Table I. Comparative Storage Technology Matrix For Farm-Scale Deployment At The Cut Farm

Technology	**Duration**	**Capital / Supply Chain**	**Fit for CUT Farm**
Li-ion battery	Hours	High; imported cells	Cycle life limits sustained use
Pumped hydro	Hours to days	Moderate; civil-heavy	Not viable, flat site
Flywheel	Seconds to minutes	High per kWh stored	Power quality only
Hydrogen storage	Hours to days	High; complex O&M	RTE penalty, skills gap
PV-A-CAES (this study)	Hours	Moderate; turbomachinery	Matches duration and lifespan

Conventional diabatic CAES, as demonstrated at the Huntorf and McIntosh utility-scale plants, vents the heat generated during compression to ambient and burns natural gas to reheat the air immediately before expansion, which caps round-trip efficiency and ties the technology to a fossil-fuel input [7]. Adiabatic CAES removes that dependency by capturing the heat of compression in a dedicated thermal energy storage (TES) medium and returning it to the expanding air during discharge, so the combustion step disappears entirely [6], [8]. Pairing that adiabatic baseline with a photovoltaic charging source, rather than off-peak grid power, defines the Solar PV Adiabatic CAES (PV-A-CAES) architecture modeled in this paper: a 90 kW system engineered specifically for the CUT Farm load profile and for Zimbabwean irradiance and geological conditions, using an above-ground pressure vessel rather than the underground salt caverns that Huntorf and McIntosh rely on.

Much of the published CAES literature addresses utility-scale plants rated in the tens to hundreds of megawatts, with dynamic and techno-economic studies calibrated to that regime and to grid-connected, off-peak charging rather than to a stand-alone photovoltaic source [9], [10]. Two gaps follow directly from that mismatch. First, comparatively little work models a decentralized, farm-scale hybrid system against the specific climatic, geological, and financial conditions of Sub-Saharan Africa, where above-ground storage, higher and more variable solar insolation, and agricultural rather than industrial load profiles all depart from the utility-scale template [1]. Second, and more fundamentally, while the steady-state thermodynamics of CAES are well documented, the transient, multi-domain behavior of a PV-charged, farm-scale system, spanning the electrical, pneumatic, thermal, and mechanical domains simultaneously, has rarely been simulated with the coupled dynamic fidelity that a controller-stability or power-quality assessment requires; Section II reviews this gap in more detail. Without a validated dynamic model, any thermodynamic optimization or downstream economic

ISSN 2278-2540 | DOI: 10.51583/IJLTEMAS | Volume XV, Issue VII, July 2026

and exergy analysis of this specific 90 kW system would rest on a steady-state foundation that cannot, by itself, confirm transient stability or the controller's ability to recover from a load disturbance.

Contribution statement: This paper closes that gap for the CUT Farm system specifically. It presents (i) a terminology-consistent, fully specified PV-A-CAES architecture sized to the farm's validated 115.63 kW load profile; (ii) a multi-domain MATLAB/Simscape model that couples the PV array and MPPT boost stage, the dual-loop FOC machine-side and grid-side converters, the intercooled compression train, the TES unit, and the radial inflow turbine within a single coupled solver rather than as separate single-domain models; (iii) transient verification of PV/MPPT settling, charging-phase pressure and thermal accumulation, and discharge-phase power, current, and torque response; and (iv) an explicit set of validated state points and power metrics, W_c = 132.7 kW, P_t = 90 kW, RTE = 67.8%, that Section V and the companion papers use directly as inputs to second-law exergy destruction mapping and Levelized-cost-of-electricity modelling, rather than re-deriving them independently.

The remainder of the paper is organized as follows. Section II reviews the historical evolution of CAES, the state of the art in PV-CAES integration and TES media, and the dynamic-simulation literature specifically, closing with an explicit statement of the gap this paper addresses. Section III describes the system architecture and the governing equations for each subsystem and domain. Section IV presents the transient simulation results, the baseline-to-optimized RTE enhancement pathway, and a comparative validation against literature benchmarks. Section V sets out the exergy and techno-economic foundations that the companion studies build on. Section VI concludes.

LITERATURE REVIEW

A. Historical Evolution of Compressed Air Energy Storage

Compressed air energy storage has a longer commercial history than most grid-scale alternatives, anchored by two operating diabatic plants. The Huntorf plant in Lower Saxony, Germany, was commissioned in 1978 with a rating of 290 MW, later augmented to 321 MW, and stores compressed air in two solution-mined salt caverns; because the heat of compression is vented to ambient and the expanding air is reheated by burning natural gas immediately ahead of the turbine, the plant's round-trip efficiency is approximately 42% [7]. The McIntosh plant in Alabama, USA, commissioned in 1991 at 110 MW, improved on that figure by adding a recuperator that recovers turbine exhaust heat to partially preheat the compressed air before combustion, raising round-trip efficiency to approximately 54% while remaining fossil-fuel dependent [6]. Both plants demonstrate CAES's multi-decade mechanical durability, but both also illustrate diabatic CAES's structural ceiling: round-trip efficiency is capped by how much of the compression heat is discarded rather than reused.

Two more architectural lines arose from this observation. Isothermal CAES achieves near-isothermal compression and expansion by keeping the heat at all times within the compression and expansion trains, instead of storing it separately, which in principle eliminates the combustion step and a separate thermal store but increases the compression and expansion trains' complexity and speed. For Adiabatic CAES, the intercooler heat is stored in an extra TES tank and is incorporated into the expanded air during discharge, thus avoiding the reheat step of using natural gas in the intercooled compression process [8] [9]. Reported round-trip efficiencies for adiabatic architectures cluster between 65% and 75%, rising toward a theoretical ceiling near 70 to 80% as TES effectiveness and turbomachinery isentropic efficiency both improve [10], [11]. The 90 kW PV-A-CAES system modeled in this paper sits within that adiabatic line, distinguished from the utility-scale, grid-charged Huntorf and McIntosh precedents by its farm scale, its above-ground pressure-vessel storage in place of a salt cavern, and its photovoltaic rather than off-peak-grid charging source.

B. State of the Art in PV-CAES Integration and Thermal Energy Storage Media

Coupling CAES with solar generation, rather than with off-peak grid power, has drawn increasing attention as a route to firming variable renewable output without a combustion step. Reported hybrid configurations range from CAES paired directly with photovoltaic arrays to more elaborate schemes that couple compressed-air

ISSN 2278-2540 | DOI: 10.51583/IJLTEMAS | Volume XV, Issue VII, July 2026

storage with concentrated solar power, using the concentrating field's thermal output to reheat the expanding air and reporting system round-trip efficiencies near 70% with exergy efficiencies above 80% [12]. Within that literature, the specific case of a farm-scale, decentralized PV-CAES system sized to an agricultural load in a Sub-Saharan African setting is not addressed; most reported hybrid PV-CAES studies target grid-connected or utility-scale configurations, leaving the farm-scale, single-owner case this paper models comparatively unexamined.

Thermal energy storage media choice is the second axis along which adiabatic architectures differ. Packed-bed sensible TES using rock, ceramic, or gravel media has been demonstrated at pilot scale, with reported thermal-storage effectiveness and cyclic performance data now available from an operating adiabatic CAES pilot plant rather than from simulation alone [13]. Packed-bed and low-temperature TES configurations have also been shown, in dynamic modelling studies of large-scale adiabatic CAES, to shift the achievable round-trip efficiency by several percentage points depending on heat-exchanger effectiveness and thermal stratification within the bed [14], [15]. The TES model used in this paper follows that packed-bed, sensible-heat approach, with heat-exchanger effectiveness raised from a 0.88 baseline to an optimized 0.92, consistent with the effectiveness gains reported for well-designed packed-bed systems in the literature reviewed here [16].

C. Dynamic Simulation Techniques: Multi-Domain Modelling Against Steady-State Thermodynamic Analysis

The majority of published CAES performance studies, including most of the historical and hybrid-configuration literature reviewed above, are steady-state thermodynamic or exergy-balance analyses: closed-form energy and entropy accounting at a fixed design point, without a time-resolved treatment of how the system reaches that point or responds to a disturbance [6], [10]. That approach is well suited to sizing and to first-law efficiency accounting, but it cannot, by construction, characterize controller stability, power-quality transients, or the coupled thermal-pneumatic-electrical response to a cloud-driven irradiance drop or a sudden agricultural load step.

A smaller body of work addresses this gap through dynamic, time-domain simulation. Sciacovelli et al. developed a fully dynamic, off-design performance model of an adiabatic CAES plant with packed-bed thermal storage, integrating algebraic and differential sub-models for the cavern, the TES, and the compression and expansion trains to link component-level and plant-level performance across successive charge and discharge cycles [17]. Luo et al. subsequently reported a feasibility study for a dedicated MATLAB/Simulink-based simulation software tool spanning the pneumatic, thermal, mechanical, and electrical domains of adiabatic CAES, validated against four case studies including grid-integration scenarios [18]. Both studies confirm that multi-physical, time-domain simulation is both feasible and necessary for transient and control-level questions that steady-state analysis cannot answer, but both are also calibrated to utility-scale plant capacities and to grid, rather than photovoltaic, charging.

This paper uses MATLAB/Simscape specifically, rather than a signal-flow Simulink block-diagram approach, because Simscape represents each subsystem as a physical network exchanging across and through variables, pressure and flow rate in the pneumatic domain, torque and angular velocity in the mechanical domain, directly with its neighbors [19]. That physical-network structure lets a single solver step advance the electrical, pneumatic, thermal, and mechanical states of the PV array, the power-electronic converters, the compression train, and the TES unit together, rather than requiring the modeler to write and maintain explicit domain-coupling equations between separately solved signal-flow subsystems, an implementation advantage that becomes material once a photovoltaic source, rather than a fixed grid connection, is added to the model.

D. Synthesis: The Gap This Paper Resolves

When combined, the literature on CAES and PV is strong on steady-state thermodynamics, and growing on utility-scale (above-ground) PV-A-CAES dynamic simulation, but not quite enough on the specific combination this paper's 90 kW CUT Farm system represents: decentralized, farm-scale, above-ground PV-A-CAES architecture, charged by a stochastic PV source rather than off-peak grid electricity, and modeled with multi-

INTERNATIONAL JOURNAL OF LATEST TECHNOLOGY IN ENGINEERING,
MANAGEMENT & APPLIED SCIENCE (IJLTEMAS)
ISSN 2278-2540 | DOI: 10.51583/IJLTEMAS | Volume XV, Issue VII, July 2026

domain transient fidelity rather than steady state, and validated through realistic Zimbabwean PV irradiances and discrete agricultural load conditions rather than idealized or utility-grid conditions [1]. This paper does this straight away. In Section III, the governing equations for each of the subsystems are presented while in Section IV, the transient behavior is reported and the validated operating point, W_c = 132.7 kW, P_t = 90 kW, RTE = 67.8%), is reported. In Section V, the exergy and techno-economic bridge is formalized, which is the basis for companion studies that are referenced throughout Section I.

SYSTEM ARCHITECTURE AND DYNAMIC MODELING METHODOLOGY

A. Subsystem Design and Multi-Domain Coupling in Simscape

Simscape allows you to represent a physical system as a network of connected components instead of as a signal-flow block diagram. For each component, it exchanges across and through variables with its neighboring components: across variables pressure and mass flow rate in pneumatic branch, temperature and heat flow in thermal branch, torque and angular velocity in mechanical branch, and voltage and current in electrical branch; across and through variables mass flow rate, temperature, torque and current [19]. The moist air domain for the pressure vessel and connecting pipework models realistically captures the behavior of compressible, humid air, and the heat transfer through the walls which determines the rate of heat exchange between the stored air and the environment. Those compressor and turbine elements, which are added to the pneumatic network, are also automatically connected to mechanical rotational elements such as shafts, torque sources and inertia, and the electrical power element, the grid-facing inverter, and the turbine generator, located in the same physical network.

Fig. 1 sets out this architecture end to end.

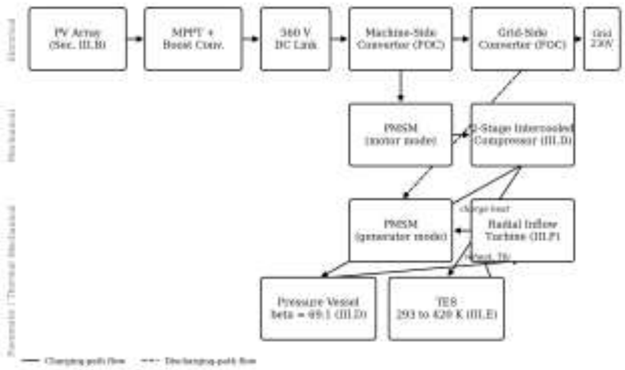

Fig. 1. System architecture: PV array and MPPT boost stage, dual-loop FOC machine-side and grid-side converters, intercooled compression train, pressure vessel and TES, and radial inflow turbine, spanning the electrical, pneumatic, thermal, and mechanical domains within a single coupled Simscape solver.

The practical consequence of this structure is that a single solver step advances the electrical, pneumatic, thermal, and mechanical states together. A charging-side disturbance, a cloud transient reducing PV output, for instance, propagates immediately through the boost converter and FOC loop into compressor torque and mass flow rate, and from there into the vessel pressure and TES thermal state, without an intermediate hand-off between separately solved models. Section III.B through III.F set out the governing equations for each subsystem in the order the energy path visits them during charging, PV array, boost converter and MPPT, FOC converters, compression train, and TES, before Section III.F covers the discharge-side turbine and reheat path that reverses that order.

B. Solar PV Array and Incremental-Conductance MPPT

The PV array is built from 330 W monocrystalline modules, 72 cells per module, open-circuit voltage 45 V, short-circuit current 9.2 A, arranged in three to four parallel strings of ten to fifteen series-connected modules to

ISSN 2278-2540 | DOI: 10.51583/IJLTEMAS | Volume XV, Issue VII, July 2026

reach the 450 to 675 VDC range the inverter stage expects. Each cell is represented by the single-diode equivalent circuit, whose terminal current follows

$$I_{PV} = I_{ph} - I_0 \cdot \left[exp\left(\frac{q\cdot(V+I\cdot R_S)}{(n\cdot k\cdot T)}\right) - 1\right] - (\frac{V+I\cdot R_S}{R_{sh}}) \quad (1)$$

where Iph is the photo-generated current, I0 the diode saturation current, q the electron charge, n the diode ideality factor, k the Boltzmann constant, T the cell temperature, and R_S and Rsh the series and shunt resistances. The array's input is the irradiance, ambient temperature, and wind speed, which are provided by a weather generator that imposes a maximum clear sky irradiance of 1000 W/m2 modified by an air mass-dependent atmospheric attenuation, a random cloud factor between 0.3 and 1.0, a diurnal irradiance curve from sunrise to sunset, and a sinusoidal variation of ambient temperature between 20 degC and 34 degC. The cloud model is stochastic and an individual day simulated can be much less than the 1000 W/m2 limit, as seen in the transient run discussed in Section IV.

The output voltage from the array is boosted to the approximate 560 V DC-link voltage required by the inverter using a boost converter. The duty cycle D of the converter is constrained by 0.08 ≤ D < 0.85 to ensure that the conversion ratio remains physically realistic and the converter's steady-state relation is

$$V_{out} = \frac{V_{in}}{(1-D)} \quad (2)$$

An Incremental Conductance algorithm sets the duty cycle, D, on the fly to track the maximum power point of the array by comparing the incremental conductance to the instantaneous conductance, and modifying the duty cycle accordingly [20],

$$\frac{dI}{dV} = -\frac{I}{V} \quad (3)$$

using a deliberately small step size, K_p = 0.002, to damp oscillation while still tracking changing irradiance, an initial duty cycle of 0.1 for smooth start-up, and voltage and convergence thresholds that keep the controller from chasing measurement noise. This is the mechanism responsible for the settling behavior of the PV current and voltage traces reported in Section IV.A.

C. Converter Architecture and Dual-Loop Field-Oriented Control

The compressor drive motor and the turbine generator are both realized as a surface-mounted Permanent Magnet Synchronous Machine (PMSM) with rated torque 111 N times m, Ld = Lq = 0.0015 H, flux linkage 0.18 Wb, and four pole pairs, connected to a 560 V DC link and limited to a maximum current of 220 A. In the synchronously rotating d-q reference frame obtained through the Clarke and Park transformations,

$$i_a = i_a, i_\beta = \frac{(i_{a+2}\cdot i_b)}{\sqrt{3}} \quad (4)$$

$$i_d = i_\alpha \cdot cos(\theta) + i_\beta \cdot sin(\theta), i_q = -i_\alpha \cdot sin(\theta) + i_\beta \cdot cos(\theta) \quad (5)$$

More generally, before specializing to the balanced two-phase form used above, the Clarke transformation maps the full three-phase stator currents onto a stationary two-axis frame together with a zero-sequence component,

$$i_a = (\frac{2}{3})i_a \cdot (\frac{1}{3})i_b \cdot (\frac{1}{3})i_c \quad (4a)$$

$$\mathrm{i}_\beta = (\frac{1}{\sqrt{3}})(\mathrm{i}_b - \mathrm{i}_c) \quad (4b)$$

$$\mathrm{i}_0 = (\frac{1}{3})(\mathrm{i}_a + \mathrm{i}_b + \mathrm{i}_c) \quad (4c)$$

ISSN 2278-2540 | DOI: 10.51583/IJLTEMAS | Volume XV, Issue VII, July 2026

using the equal-amplitude convention, which preserves peak current magnitude between the three-phase and two-phase representations rather than instantaneous power. Under the balanced, wye-connected winding assumed throughout this paper, $i_a + i_b + i_c = 0$ at every instant, so i_0 vanishes identically and the two-term form of Eq. (4) used above is exact rather than approximate. The Park transformation of Eq. (5) then rotates this stationary alpha-beta frame by the instantaneous electrical rotor angle, $\theta_{e(t)}$, the running integral of ω_e, so that under balanced sinusoidal excitation the d- and q-axis quantities settle to constant values rather than oscillating at the electrical frequency. It is this property, not the coordinate change by itself, that lets the proportional-integral current controllers introduced below regulate i_d and i_q against a fixed reference rather than a moving sinusoidal target.

the stator voltage dynamics that Field-Oriented Control regulates are the coupled differential state equations [21]

$$v_d = R_s \cdot i_d + L_d \cdot \left(\frac{di_d}{dt}\right) - \omega_e \cdot L_q \cdot i_q \qquad (6)$$

$$v_q = R_s \cdot i_q + L_q \cdot \left(\frac{di_q}{dt}\right) + \omega_e \cdot L_d \cdot i_d + \omega_e \cdot \lambda_m \quad (7)$$

where R_s is the stator resistance and ω_e the electrical rotor speed. The cross-coupling terms, minus $\omega_e \cdot L_q \cdot i_q$in the d-axis equation and plus $\omega_e \cdot L_d \cdot i_d$ in the q-axis equation, are exactly what the feed-forward decoupling in the current controllers exists to cancel, so that i_d and i_q can be regulated as if the two axes were independent first-order systems.

That claim is not merely qualitative. Writing the commanded d-axis voltage as the PI output plus the feed-forward term, $v_{d*} = \left(\frac{K_p+K_i}{s}\right)(i_{d*} - i_d) + \omega_e \cdot L_q \cdot i_q$, and substituting v_{d*} for v_d in Eq. (6) cancels the cross-coupling term exactly, leaving a single-input, single-output plant on each axis,

$$L_d \cdot \left(\frac{di_d}{dt}\right) + R_s \cdot i_d = \left(\frac{K_p+K_i}{s}\right)(i_{d*} - i_d) \qquad (7a)$$

Taking the Laplace transform and solving for the closed-loop transfer function gives the standard second-order current-loop response,

$$\frac{I_d(s)}{I_d*(s)} = \left(\frac{K_p s+K_i}{(L_d s^2+(R_s+K_p)s+K_i}\right) \qquad (7b)$$

A standard tuning choice for this structure sets the integral-to-proportional gain ratio to cancel the plant's own electrical pole, $\frac{K_i}{K_p} = \frac{R_s}{L_d}$; under that condition Eq. (7b) collapses to a clean first-order response,

$$\frac{I_d(s)}{I_d*(s)} = \frac{\omega_e}{(s+\omega_c)}, \omega_c = \frac{K_p}{L_d} \qquad (7c)$$

which is the independent first-order behavior assumed above. With the $K_p = 2$ and $L_d = 0.0015$ H used for the machine-side current loop in this section, Eq. (7c) places the closed-loop bandwidth at $\omega_c = \frac{K_p}{L_d}$, approximately 1333 rad/s, near 212 Hz, an order of magnitude below the 10 kHz switching frequency and fast enough that the current loop does not constrain the sub-100 ms settling reported in Section IV.A. The q-axis loop follows the same derivation with L_q in place of L_d.

Electromagnetic torque and rotor mechanical dynamics follow as

$$T_e = 1.5 \cdot P \cdot [\lambda_m \cdot i_q + (L_d - L_q) \cdot i_d \cdot i_q] \qquad (8)$$

$$J \cdot \left(\frac{d\omega_m}{dt}\right) = T_e - T_L - B \cdot \omega_m \qquad (9)$$

ISSN 2278-2540 | DOI: 10.51583/IJLTEMAS | Volume XV, Issue VII, July 2026

with J the combined rotor and coupled-load inertia, B the viscous damping coefficient, and TL the load torque presented by the compressor or, during discharge, by the turbine.

A Field-Oriented Control loop, sampled every 100 microseconds, a 10 kHz switching frequency, uses proportional-integral current controllers, $K_p = 2$, $K_i = 100$, on both axes, with the feed-forward decoupling terms above and integrator anti-windup limited to plus or minus $\frac{V_{dc}}{2}$ to keep the loop stable through transients. The resulting voltage commands pass through inverse Park and Clarke transformations and are applied with Space Vector PWM, which uses a zero-sequence offset to maximize DC-bus utilization [22]; the maximum phase voltage the converter can produce is

$$V_{max} =\cdot 0.577V_{dc} \qquad (10)$$

which for the 560 V link gives roughly 323 V. On the grid side, the Grid-Side Converter runs an outer voltage loop that holds the DC link at its 560 V reference, K_p, v = 0.5, K_i, v = 10, with the resulting current reference limited to plus or minus 400 A, and an inner current loop, K_p, i = 5, K_i, i = 200, that regulates active and reactive power independently, with the reactive-axis reference held at zero so the system exports power at unity power factor into the 230 V, 50 Hz grid. Together, the machine-side and grid-side loops let the same converter architecture drive the compressor as a motor during charging and absorb the turbine's output as a generator during discharge.

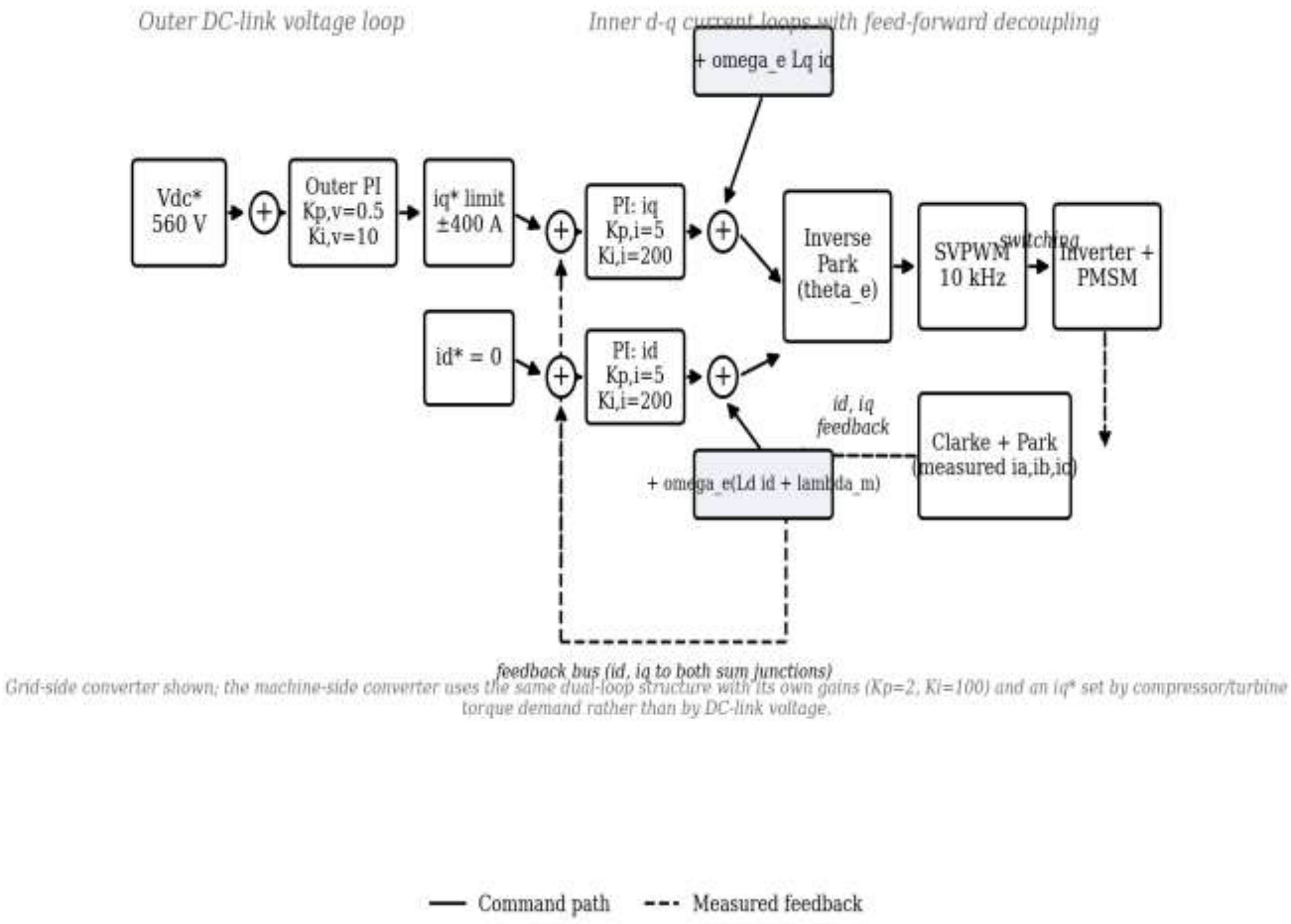

Fig. 2. Dual-loop Field-Oriented Control structure. The grid-side converter is shown; the machine-side converter follows the same outer and inner architecture with the gains derived in Eq. (7c) and an iq reference set by compressor or turbine torque demand rather than by DC-link voltage.

ISSN 2278-2540 | DOI: 10.51583/IJLTEMAS | Volume XV, Issue VII, July 2026

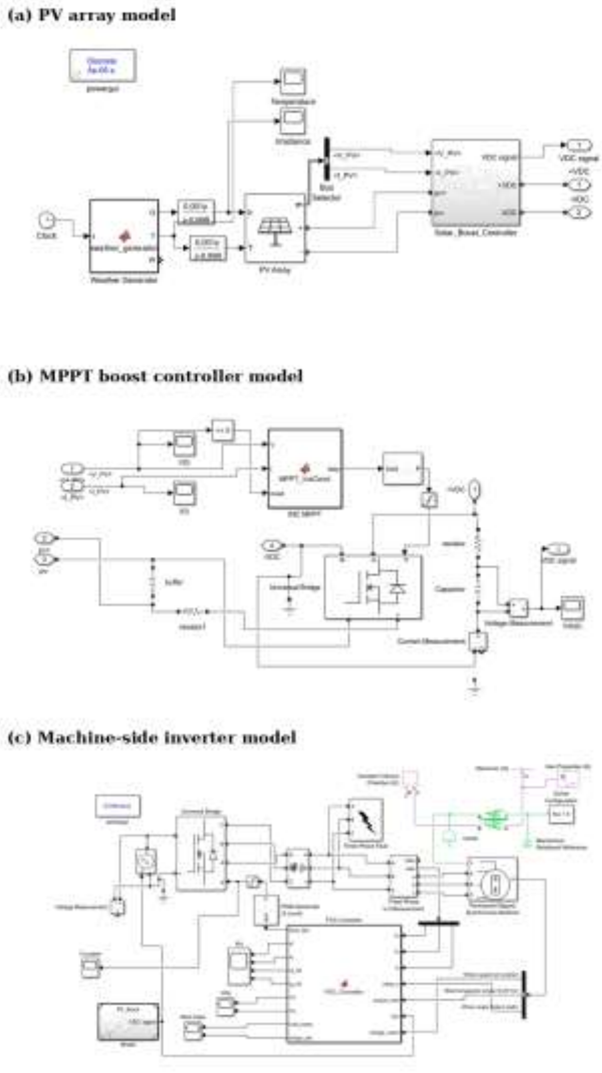

Fig. 3. Simscape model canvases: (a) PV array, (b) incremental-conductance MPPT boost controller, (c) machine-side inverter.

D. Charging Train Thermodynamics: Multi-Stage Intercooled Compression

During charging, a compressor rated at 150 kW draws ambient air at 1 bar and 298.15 K and raises it toward the storage pressure through a sequence of intercooled stages. For the i-th compression stage, with pressure ratio β_c, i and inlet temperature T_c, i,in, the outlet temperature and specific work follow from the polytropic relation as

$$T_c, i_{out} = T_c, i_{in} \cdot [1 + \frac{(\beta_c, i^{\frac{(k-1)}{k}} - 1)}{\eta_c}] \qquad (11)$$

$$w_c, i = T_c, i_{in} \cdot [\frac{(\beta_c, i^{\frac{(k-1)}{k}} - 1)}{\eta_c}] \qquad (12)$$

with a heat capacity ratio k = 1.4 and cp = 1005 J/(kg K) throughout. Raising the isentropic efficiency η_c from a 0.82 baseline to an optimized 0.88, through multi-stage intercooling and an advanced centrifugal impeller geometry, narrows the temperature rise across each stage and reduces internal aerodynamic losses. Summed over the intercooled stages at the design mass flow rate G_c = 0.247 kg/s, the total compression power comes to

$$W_c = G_c \cdot \sum w_c, i \approx 132.7 \text{ kW} \qquad (13)$$

INTERNATIONAL JOURNAL OF LATEST TECHNOLOGY IN ENGINEERING, MANAGEMENT & APPLIED SCIENCE (IJLTEMAS)
ISSN 2278-2540 | DOI: 10.51583/IJLTEMAS | Volume XV, Issue VII, July 2026

matching the validated W_c = 132.7 kW operating point used throughout this paper and its companion analyses.

Between compression stages, an intercooler transfers the heat of compression into the TES medium rather than rejecting it to ambient. If T_c, i_{out} is the outlet temperature of stage i and ε_c is the heat-exchanger effectiveness, the inlet temperature entering stage i+1 is

$$T_{c,(i+1),in} = \varepsilon_c \cdot T_{(i+1)f} + (1 - \varepsilon_c) \cdot T_{c,i,out} \qquad (14)$$

Optimizing this exchanger geometry raises ε_c from 0.88 to 0.92. The mass of air accumulated in the above-ground storage vessel obeys the simple charging balance

$$\frac{dm}{dt} = G_c(t) \qquad (15)$$

and the vessel pressure is obtained at each time step from the ideal gas law applied to the accumulated mass and the vessel's own thermal state,

$$P(t) = m(t) \cdot R_{air} \cdot \frac{T(t)}{V} \qquad (16)$$

with V the fixed vessel volume and R_{air} = 287.1 J/(kg K) the specific gas constant for air. Integrating Eq. (16) against the compressor's mass flow over the 6-hour charging window, subject to a safety cut-off at the design pressure ceiling, is what produces the pressure trajectory examined in Section IV.B. This design ceiling, which is the overall pressure ratio β_{total} = 69.1 as given in Section III, is used throughout the rest of this paper. The companion exergy analysis indicates that the design pressure ceiling is approximately 70 bar, and it is used in the same manner as in that analysis in the present work. Within the range of simulated time, the vessel pressure does not come close to attaining that ceiling, consistent with a partial charge cycle.

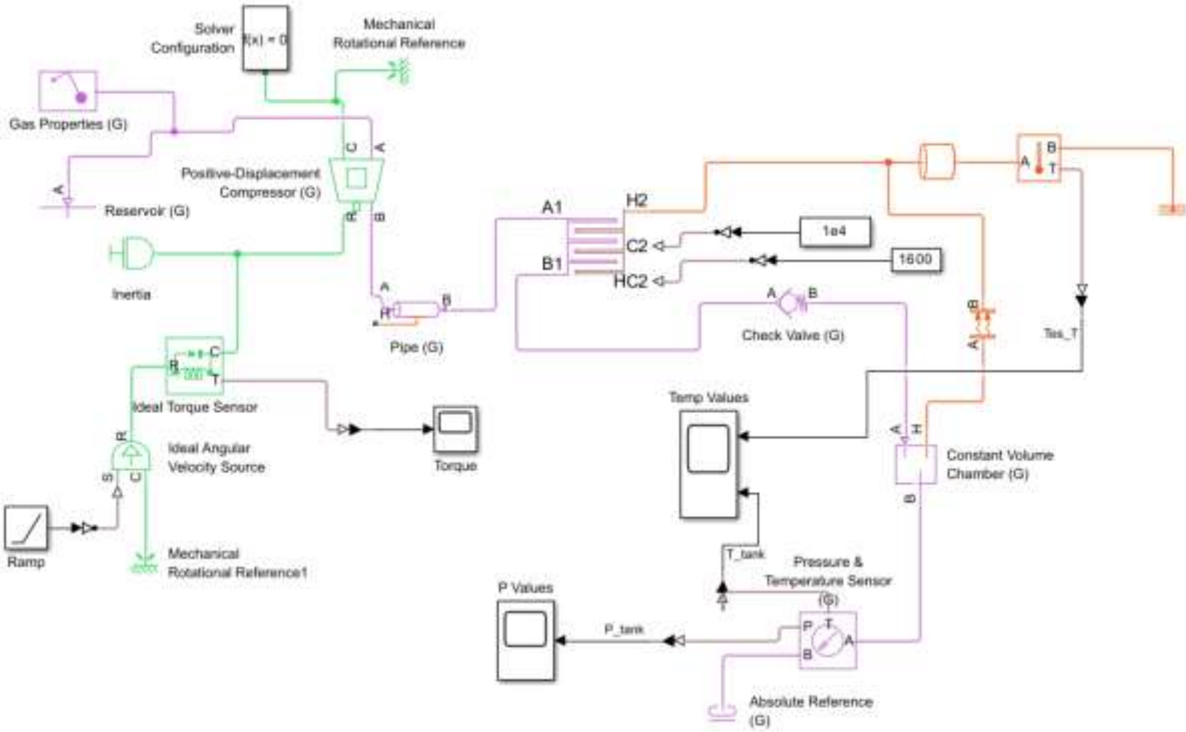

Fig. 4. Simscape charging subsystem model: compressor, intercooler and TES coupling, and vessel.

E. Thermal Energy Storage Modeling: Transient Heat Balance

It is assumed that the TES medium has a thermal capacity of 2.76 MJ/K, sized at 3072 kg and specific heat of 900 J/Kg K, and exchanges heat with the compressor intercooler stream during charging and with the turbine

ISSN 2278-2540 | DOI: 10.51583/IJLTEMAS | Volume XV, Issue VII, July 2026

reheat stream during discharging. It is assumed that its transient temperature will follow the lumped-capacitance energy balance.

$$M_{TES} \cdot C_{p,TES} \cdot \left(\frac{dT_{TES}}{dt}\right) = Q_{in,c}(t) - Q_{out,d}(t) - Q_{loss} \qquad (17)$$

where $Q_{in,c}(t)$ is the instantaneous heat rate delivered by the intercooler during charging, $Q_{out,d}(t)$ is the heat rate withdrawn to reheat the discharge air, and Q_{loss} is a small parasitic loss term to ambient through the vessel insulation. During the charging window, Eq. (17) integrates from the 293 K ambient starting condition and, over the six hours examined in Section IV.B, reaches a peak of approximately 589 K as the TES medium absorbs the heat of compression; this is distinct from the T_{fa} = 420 K reheat target validated in Section III.F and reused identically as the TES-side state point in the companion exergy analysis, which characterizes the temperature the discharge-side reheat process delivers to the turbine inlet rather than the TES medium's own peak thermal-mass temperature during charging. Discharge draws this stored heat back down through the same balance, $Q_{out,d}(t)$ now dominating, as the reheat stage described in Section III.F pulls the TES medium's temperature back toward its charging-window minimum ahead of the next cycle.

F. Discharging Train Thermodynamics: Reheat and Radial Inflow Turbine Expansion

On discharge the energy path is reversed, with the additional step of thermal recovery which is missing from charging. The TES reheats the air before high pressure air is released from the storage vessel to the turbine to prevent icing and to preserve turbine efficiency, since the cooling process takes place at low temperature. This air then expands from the vessel pressure to the ambient (atmospheric) pressure through a radial inlet turbine. The isentropic turbine exit temperature for the representation of a single stage turbine is

$$T_{2s} = T_1 \cdot \left(\frac{P_2}{P_1}\right)^{\left\{\frac{(y-1)}{y}\right\}}, T_1 = T_{fa} = 420K \qquad (18)$$

The actual exit temperature follows the same relation between isentropic efficiency and turbine efficiency as the turbulent isentropic efficiency is increased from 0.86 to 0.92 by the same modifications done to the blade geometry on a radial-inflow turbine. This equivalent single-stage model covers the entire β_{total} = 69.1 ratio which the real two stage model only reaches when aggregated, so that it is not a physical temperature measured by either real stage but rather a "bookkeeping" temperature; the work it performs is specifically defined by the validated discharge power and mass flow rate.

$$T_2 = T_{1-\eta t} \cdot \left(T_{1-T_2 s}\right) \qquad (19)$$

$$w_t = \frac{P_t}{G_b} = \frac{90}{0.276} \approx 325.9 \text{ kJ/kg} \qquad (20)$$

so that the turbine delivers

$$P_t = G_b \cdot w_t \approx 90kW \qquad (21)$$

at the design mass flow rate, matching the rated discharge power of the system. A practical rotor for this duty falls in the 0.25 to 0.35 m diameter range, spinning between 15,000 and 30,000 rpm.

Because the physical machine has two expansion stages in series, an equivalent single-stage parameterization is used to preserve the correct total specific work. At the full system pressure ratio β_{total} = 69.1, the equivalent single-stage turbine efficiency is $\eta_t \approx 0.92$, matching the per-stage isentropic efficiency established earlier in this section.

This single-stage parameterization preserves the defining thermodynamic feature of adiabatic CAES operation, discharge sustained entirely by stored compression heat, with no supplementary firing required at any point in

INTERNATIONAL JOURNAL OF LATEST TECHNOLOGY IN ENGINEERING, MANAGEMENT & APPLIED SCIENCE (IJLTEMAS)
ISSN 2278-2540 | DOI: 10.51583/IJLTEMAS | Volume XV, Issue VII, July 2026

the cycle, and it is this same β_{total} = 69.1 operating point, together with G_c = 0.247 kg/s, G_b = 0.276 kg/s, and T_{fa} = 420 K, that Section V carries forward as the shared basis for the exergy and techno-economic bridge.

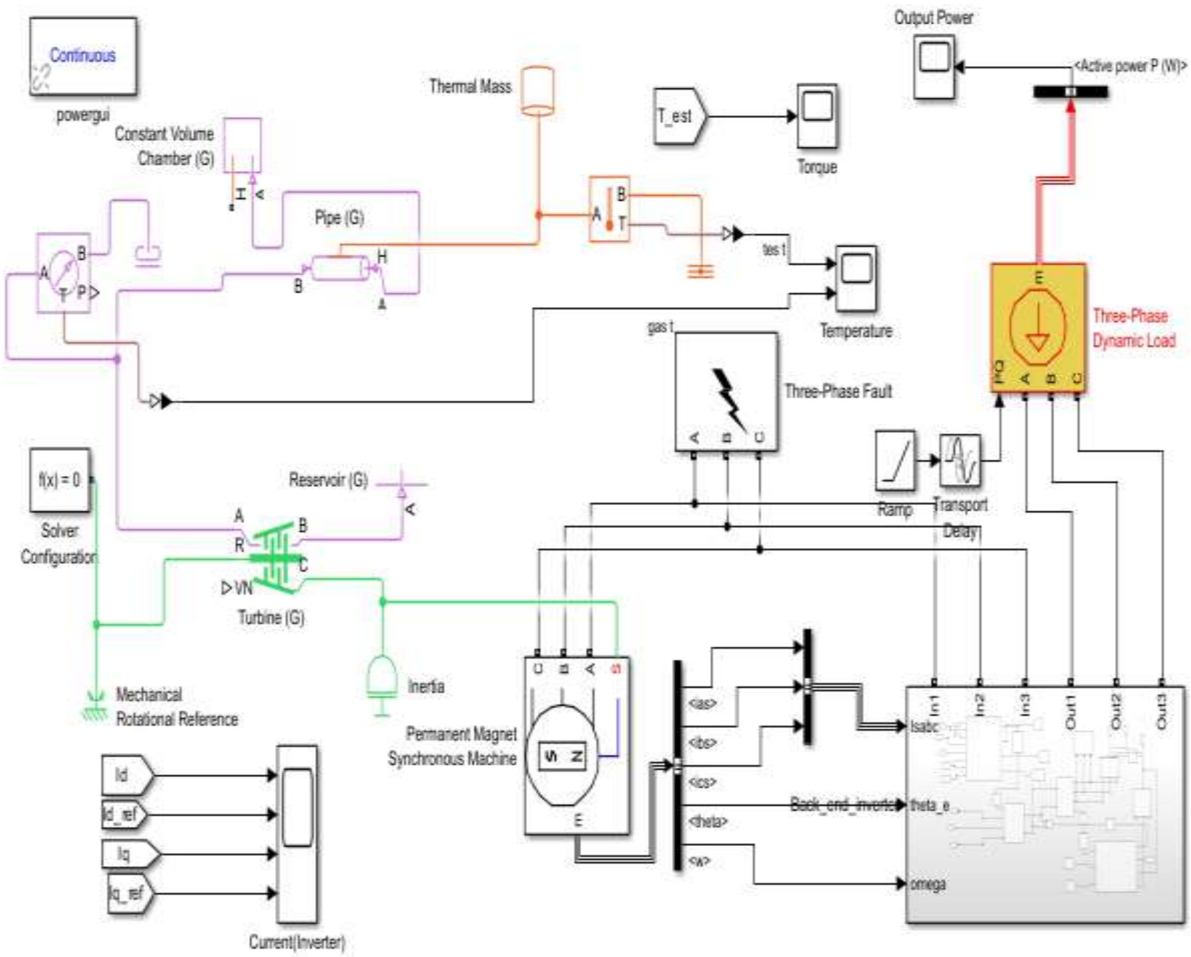

Fig. 5. Simscape discharging subsystem model: TES reheat, turbine, and generator coupling.

SIMULATION SETUP, TRANSIENT RESULTS, AND TECHNICAL DISCUSSION

A. Power Electronics and MPPT Response

The simulated day begins with zero irradiance overnight, rises from around 06:00, and peaks near 600 W/m2 in the early afternoon before falling away toward dusk, a trace shaped by the stochastic cloud attenuation in the weather generator rather than by the 1000 W/m^2 clear-sky ceiling the model allows for. PV current tracks that irradiance profile with a brief inrush to about 80 A at sunrise, produced by the momentary absence of the opposing internal resistance that limits steady operation, before settling to a stable 22 A for the remainder of the daylight hours; PV voltage follows a similar pattern, rising sharply toward the array's operating point and stabilizing just under 700 V. The Incremental Conductance MPPT algorithm of Section III.B is what keeps this settling behavior clean rather than oscillatory. From the simulations below in Fig 6, it can be noted that the run time of 240ms represents one full day of 24 hours.

ISSN 2278-2540 | DOI: 10.51583/IJLTEMAS | Volume XV, Issue VII, July 2026

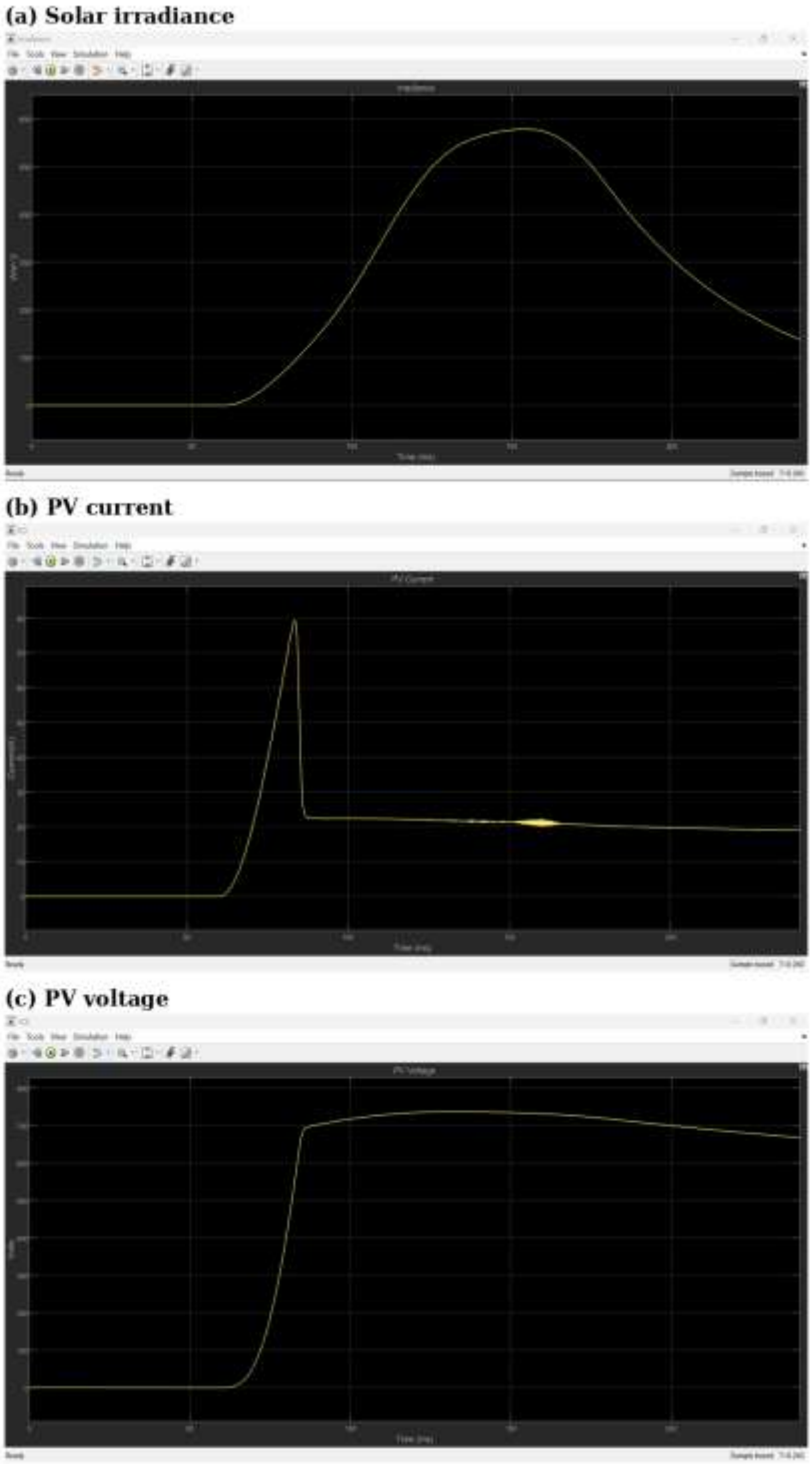

Fig. 6. Simulated PV subsystem transients: (a) solar irradiance, (b) PV current, (c) PV voltage.

The FOC loop shows a comparable pattern on the electrical side: the d-q currents and voltages exhibit a brief transient and oscillatory period at start-up, consistent with controller initialization against the state equations of Section III.C, before damping out within roughly 50 to 100 ms. The d-axis voltage settles near 0 V and the q-axis voltage settles near 3.7 V, both consistent with stable field-oriented decoupling under light loading. Together, the PV and FOC transients confirm that the power-electronic front end reaches a well-controlled steady state quickly enough not to constrain the slower thermodynamic dynamics that follow.

ISSN 2278-2540 | DOI: 10.51583/IJLTEMAS | Volume XV, Issue VII, July 2026

(a) Inverter Idq currents

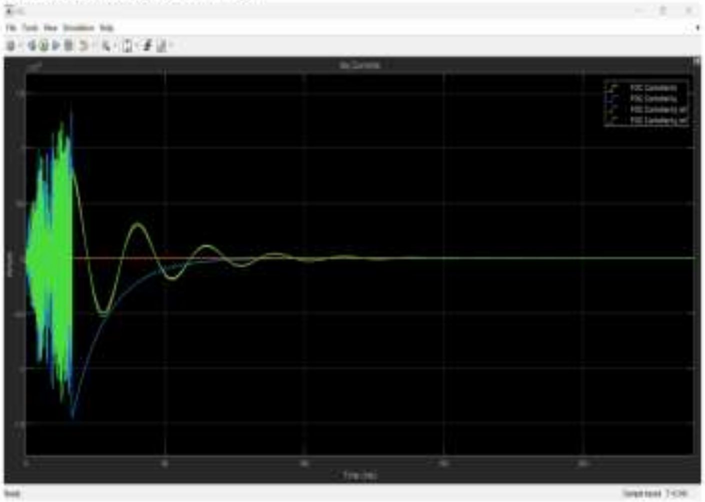

(b) Inverter Vdq voltages

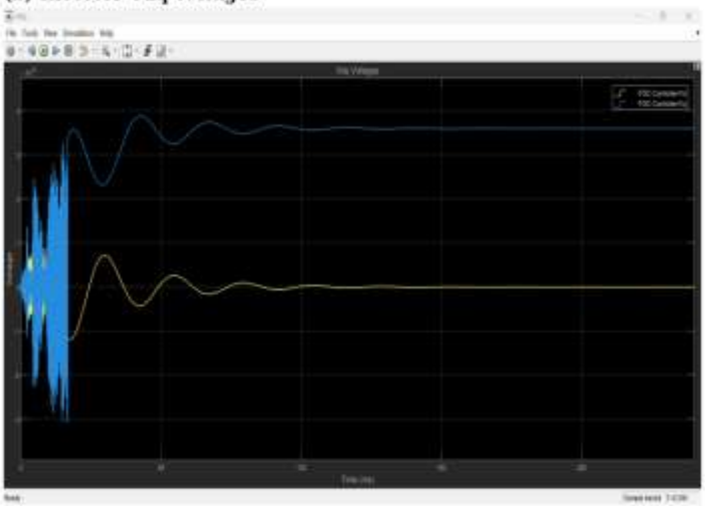

Fig. 7. Machine-side FOC transients: (a) Idq currents, (b) Vdq voltages. From the simulations above in Fig 7, it can be noted that the run time of 240ms represents one full day of 24 hours.

B. Charging-Phase Dynamics: Pressure, Torque, and Thermal Storage Response

During the six-hour charging time, the pressure difference increases from atmospheric towards the desired state of the vessel, and the integral of Eq (16) is calculated over the mass flow rate of the compressor defined in Section III.D. The increase is gradual throughout the first half of the window and increases as the compressor works against a higher back-pressure in the second half, to only 8.412 bar which is well below the design of approximately 70 bar for β_{total} set in Section III. However, the six-hour window modeled here is only a portion of a full pressure design charge cycle, so these results represent a partial-charge condition, not the fully charged state. The overall shape is similar to compressor torque, with a near zero start to a high peak in the late charging window, and then a high compressor torque to help move the compressor through the increasing tank pressure. Statistics in the charging-phase are summarized in Table I.

Table I. Simulated Charging-Phase Statistics For Vessel Pressure and Tes Temperature, Six-Hour Window

Statistic	**Vessel Pressure (bar)**	**TES Temperature (K)**
Maximum	8.412	589.0
Minimum	1.013 (atmospheric)	293.2 (ambient)

ISSN 2278-2540 | DOI: 10.51583/IJLTEMAS | Volume XV, Issue VII, July 2026

Mean	3.481	391.7
Median	2.863	367.0
RMS	4.122	401.6

Note: statistics computed over the six-hour simulated charging window. The vessel's design pressure ratio, β_{total} = 69.1, approximately 70 bar, and the discharge-side reheat target, T_{fa} = 420 K, are separate design-basis parameters defined in Section III.D through III.F and carried forward to the exergy and techno-economic bridge in Section V, not results of this specific transient window.

a. Cavern pressure

b. TES Temperature

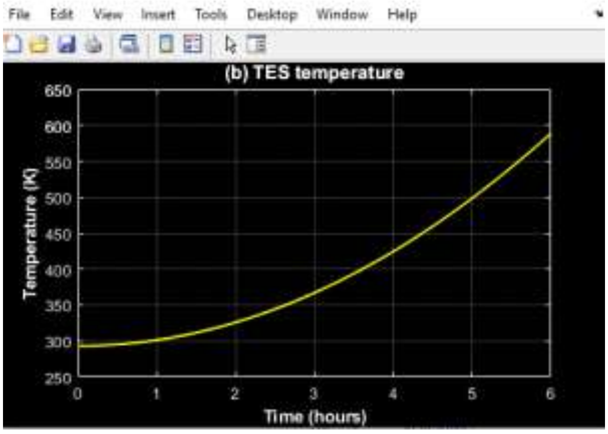

c. How the system charges over the 6-hour window?

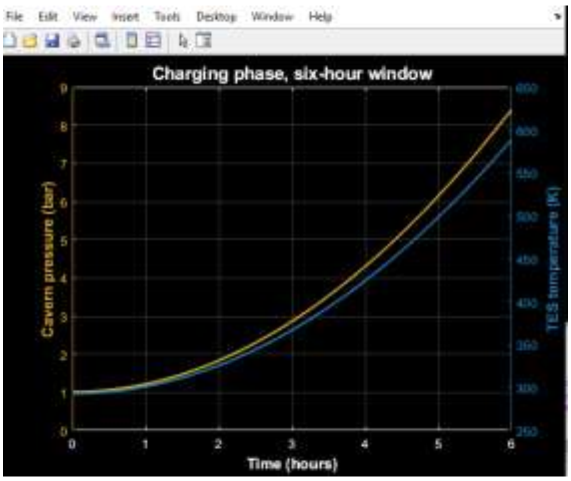

INTERNATIONAL JOURNAL OF LATEST TECHNOLOGY IN ENGINEERING,
MANAGEMENT & APPLIED SCIENCE (IJLTEMAS)
ISSN 2278-2540 | DOI: 10.51583/IJLTEMAS | Volume XV, Issue VII, July 2026

Fig. 8. Charging-phase scope traces: (a) cavern pressure, (b) TES temperature, (c) 6-hour charging window

The temperature profile of the TES is raised continuously during the same window, starting from the ambient conditions of 293 K, all the way to a peak of 589 K, corresponding to heat of compression accumulated by the intercooler stages outlined in Section III.D. This trace does not show any oscillation, which means a good coupling between the compressed air and TES medium and is key to achieving the round-trip efficiency result reported in Section IV. This is expected, as it is the heat recovered here that would be returned to the turbine inlet during discharge. From the simulations above in Fig 8, the simulations were done using a real-world time of 6 hours.

C. Discharging-Phase Dynamics: Power, Current, and Torque Response

The output power increases in a controlled ramp (nearly linear) from a near zero 'start' region, where the compressed air pressure and the turbine conditions are still settling out, to a constant 90 kW during discharge. This trace does not show any abrupt changes or oscillation which shows that the mass flow rate and expansion pressure are well matched to the operating envelope of the turbine and to the TES reheat supply of Section III.F, to prevent the mechanical stress that a more erratic ramp would put on the turbine/generator.

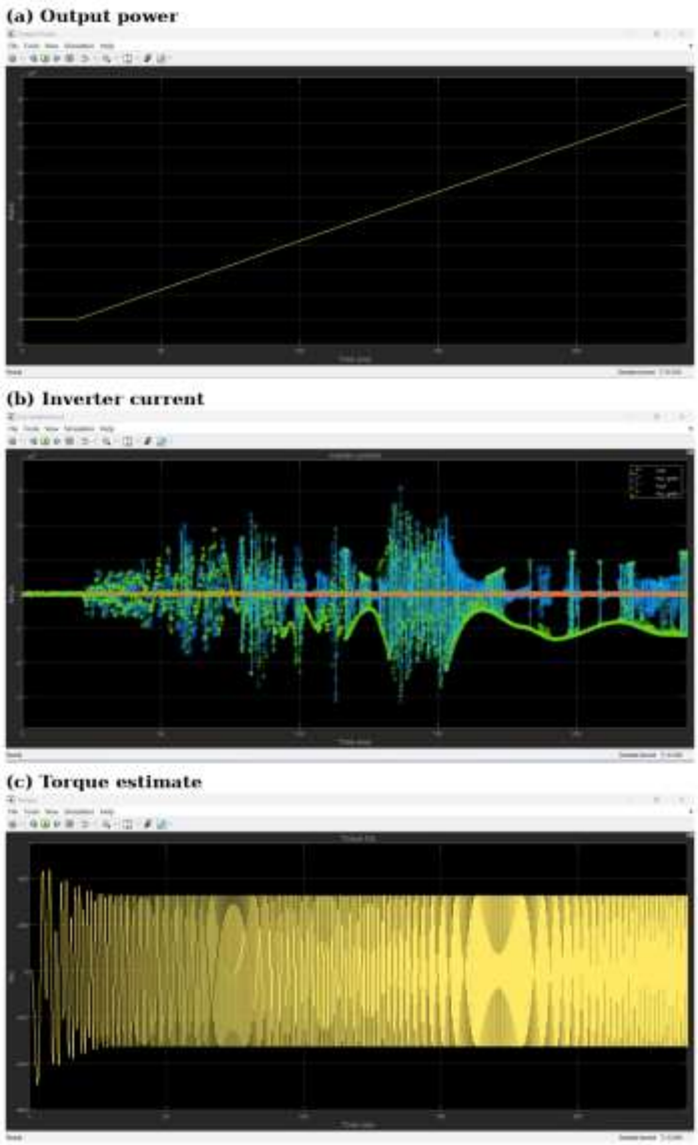

Fig. 9. Discharge-phase scope traces: (a) output power, (b) inverter current, (c) torque estimate.

The current and torque curve traces are not as smooth in opening seconds of the discharge. The current in the d-axis is relatively small during the start-up, showing little oscillation, whereas the phase current oscillations are

ISSN 2278-2540 | DOI: 10.51583/IJLTEMAS | Volume XV, Issue VII, July 2026

prominent throughout the start-up process, as the grid, the inverter switching, and the turbine-generator interact during the start-up. Electromagnetic torque, calculated from Eq. (10), is similar, with a large initial swing of ~ 450 N times m settling to a final value of ~ 320 N times m as the pressure, speed and electrical loading approach each other. This is an alternating torque ripple that continues after the start and is not due to instability, but to inverter switching and the overall picture is one of controlled load-following discharge rather than an unstable start-up. From the simulations above in Fig 9, it can be noted that the run time of 240ms represents one full day of 24 hours.

D. Round-Trip Efficiency Enhancement Pathway

System round-trip efficiency is defined as the ratio of net electrical energy delivered at the grid during discharge to the electrical energy consumed by the compression train during charging,

$$\eta_{RTE} = \frac{P_t}{W_c} \text{ x } 100\% = \frac{90}{132.7} \text{ x } 100\% = 67.8\% \quad (22)$$

This 67.8% result represents an 18.8 percentage point gain over a 49.0% diabatic baseline, and that gain resolves cleanly into the three targeted improvements described in Section III: compressor optimization contributes 6.4 percentage points, turbine optimization contributes 7.2 percentage points, and the improvement in TES heat-exchanger effectiveness contributes the remaining 5.2 percentage points. Table II sets out the baseline and optimized parameters side by side.

TABLE II. THERMODYNAMIC DESIGN PARAMETERS, BASELINE VERSUS OPTIMIZED 90 kW PV-A-CAES SYSTEM

Parameter	**Baseline**	**Optimized**
Rated discharge power, P_t (kW)	90	90
Compression power input, W (kW)	161	132.7
Compressor isentropic efficiency, η_c	0.82	0.88
Turbine isentropic efficiency, η_t	0.86	0.92
TES heat-exchanger effectiveness, e	0.88	0.92
Turbine inlet temperature, T_{fa} (K)	420	420
Overall pressure ratio, β	69.1	69.1
Round-trip efficiency, RTE	49.0%	67.8%

ISSN 2278-2540 | DOI: 10.51583/IJLTEMAS | Volume XV, Issue VII, July 2026

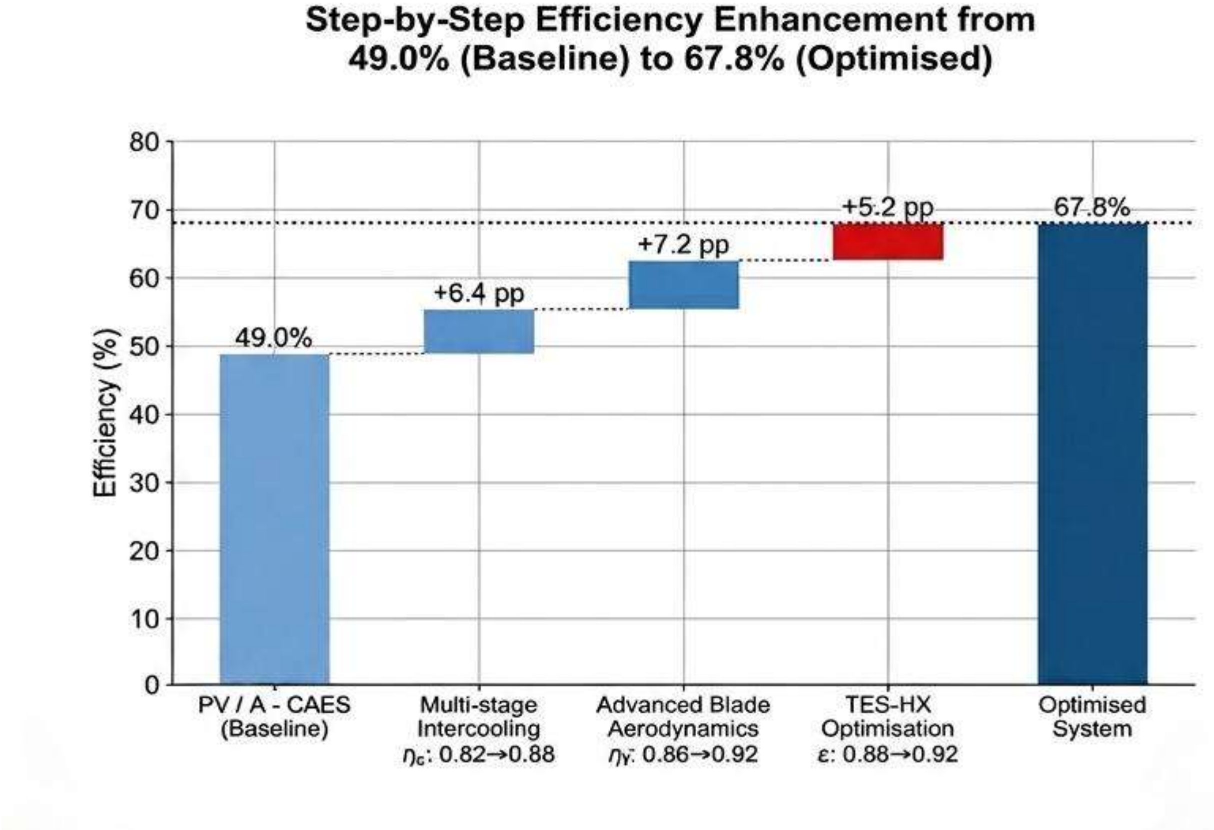

Fig. 10. Round-trip efficiency enhancement pathway from the 49.0% diabatic baseline to the 67.8% optimized PV-A-CAES result, decomposed into compressor, turbine, and TES contributions.

E. Literature Validation and Sensitivity and Uncertainty Bounds

The simulated 67.8% RTE is checked here against the two operational CAES plants and against ranges reported for adiabatic and PV-CAES systems in the literature, summarized in Table III.

Table Iii. Comparative Validation of Simulated Round-Trip Efficiency Against Physical Plant Benchmarks

System / Reference	RTE	Notes
Huntorf, Germany (diabatic, 1978)	42%	No heat recovery, gas reheat required
McIntosh, USA (diabatic, 1991)	54%	Recuperator added, still fossil-fuel dependent
Adiabatic CAES ceiling (literature)	70 to 80%	Upper bound for adiabatic architectures
PV-CAES hybrids without TES (global)	40 to 55%	No thermal energy storage integration
This study, CUT Farm 90 kW PV-A-CAES	67.8%	TES heat recovery, optimized ratios, Simscape dynamic model

Against the Huntorf baseline, the simulated result is about 61% higher in relative terms, 67.8% versus 42%, and it clears the upper end of the 40 to 55% range reported for PV-CAES hybrids that lack TES integration by roughly a quarter. It also falls within the 65 to 75% band reported for optimized above-ground adiabatic

ISSN 2278-2540 | DOI: 10.51583/IJLTEMAS | Volume XV, Issue VII, July 2026

installations in Section II.A, and it approaches, though it remains just under, the lower bound of the 70 to 80% theoretical ceiling for adiabatic architectures. The shortfall against that ceiling is consistent with the irreversibilities inherent to an above-ground pressure vessel, which does not benefit from the geological thermal mass that an underground salt cavern provides, a reasonable trade-off for a farm-scale, above-ground prototype. The TES subsystem is the main contributor to this performance: by capturing and returning the heat of compression at the effectiveness established in Section III.E, it removes the fossil-fuel reheat penalty that limits diabatic CAES, while the FOC-based energy management system of Section III.C keeps the DC bus stable and matches compressor loading to the available PV generation, further reducing off-design losses.

A number of simplifying assumptions accompany the results above, and they are recorded here so the 67.8% figure is read correctly. The storage vessel is modeled as perfectly sealed, whereas a physical above-ground vessel rated for the β_{total} = 69.1 design duty would leak at an estimated 0.1 to 0.5% per day. Irradiance profile has been idealized, with smooth ramps; in reality, cloud transients at the CUT Farm site would result in sub-minute irradiance drops that would potentially cause a compressor to cycle and would cause an estimated 2-4% drop in RTE. Ambient temperature is maintained at 25 degC although in Zimbabwe summer days can reach 35 degC, which would reduce the PV module efficiency by about 4-5% and slightly affect the compression ratios. Isentropic efficiencies have a manufacturer test variance of approximately ±3-5%, and the TES thermal mass and thermal effectiveness have a conservative uncertainty of ±5%, as some phase-change behaviors and thermal stratification are not represented in the model. These bounds can be combined by worst-case additive analysis, yielding a range of about 61.0% to 67.8% for the expected physical-prototype RTE, with the simulated 67.8% value representing an ideal upper bound; even at the conservative lower bound, this system is well above the 42% Huntorf diabatic floor.

Exergy And Economic Foundations: A Bridging Section

A. Exergy Analysis Foundation

The validated dynamic operating point established in Sections III and IV is expressed here as a set of thermodynamic state points so that the companion second-law study can compute entropy generation and exergy destruction directly, without re-deriving the underlying dynamic model. For a stream at temperature T, pressure P, specific enthalpy h, and specific entropy s, referenced to the dead state (T_0 = 293 K, h_0, s_0), the specific flow exergy is [23]

$$e_x = (h - h_0) - T_0 \cdot (s - s_0) \qquad (23)$$

Eq. (23) follows from combining the steady-flow energy balance with the entropy balance for an open system exchanging heat with the environment at T0. For a control volume with one inlet and one outlet, the first law gives $q - w = (h_{out} - h_{in})$ and the second law gives $S_{gen} = (s_{out} - s_{in}) - \frac{q}{T_0}$ greater than or equal to 0; eliminating the heat interaction q between these two balances and multiplying the resulting entropy-generation term by T_0 recovers the Gouy-Stodola relation linking real, irreversible work to its reversible ideal,

$$w_{actual} = w_{reversible - T_0} S_{gen} \qquad (23a)$$

so that the exergy any real process destroys is directly proportional to the entropy it generates,

$$i_x = T_0 S_{gen} \qquad (23b)$$

a result the companion second-law study applies component by component rather than to the cycle as a whole. Applied to a single compression stage, the exergy balance relates the actual work supplied to the flow-exergy rise of the air plus the destruction the stage incurs,

$$w_{c,i} = \left(e_{x,out} - e_{x,in}\right) + i_{x,c,i} \qquad (23c)$$

INTERNATIONAL JOURNAL OF LATEST TECHNOLOGY IN ENGINEERING, MANAGEMENT & APPLIED SCIENCE (IJLTEMAS)
ISSN 2278-2540 | DOI: 10.51583/IJLTEMAS | Volume XV, Issue VII, July 2026

so the compressor's second-law efficiency is the ratio of the reversible-minimum work to the work actually supplied,

$$\psi_c = \frac{(e_{x,out} - e_{x,in})}{w_{c,i}} \quad (23d)$$

The turbine balance inverts this comparison, since the machine now extracts work from a decaying exergy flow rather than adding to a rising one,

$$\psi_t = \frac{w_t}{(e_{x,in} - e_{x,out})} \quad (23e)$$

while the TES heat exchanger, which transfers heat rather than shaft work between the compressor-side and TES-side streams, destroys exergy in proportion to the temperature difference driving that transfer,

$$i_{x,TES} = T_0 \cdot \left[(s_{c,out} - s_{c,in}) - (s_{h,in} - s_{h,out}) \right] \quad (23f)$$

with the subscripts h and c denoting the hot, compressor-side, and cold, TES-side, streams of the intercooler. Equations (23c) through (23f), together with the state points of Table IV, are what let the companion second-law study resolve the residual gap between this paper's 67.8% round-trip efficiency and an ideal reversible cycle into separate compressor, turbine, and heat-exchanger contributions, rather than leaving it as the single undifferentiated figure Section IV.D reports.

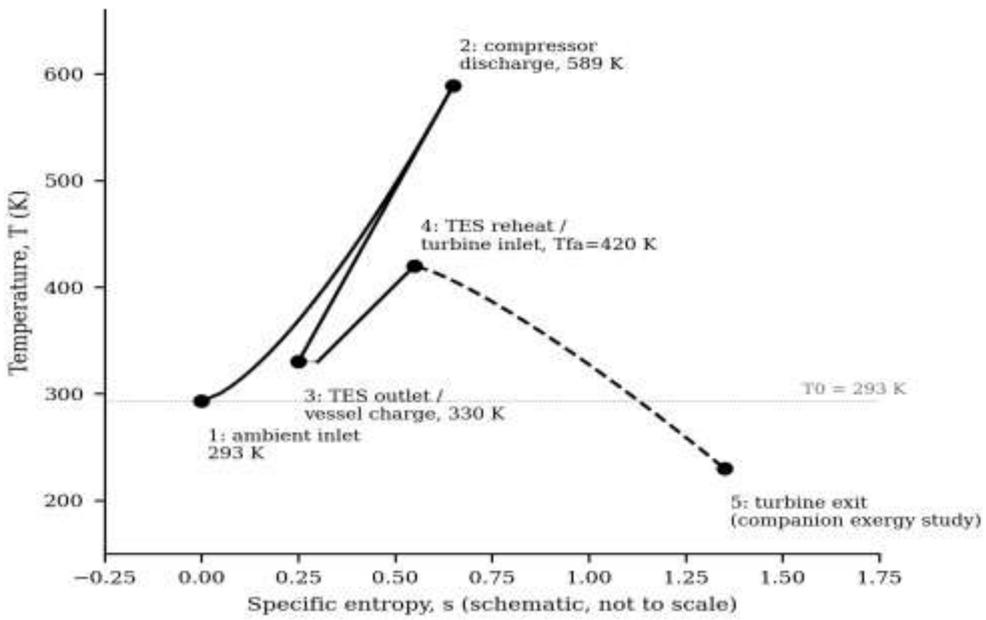

Fig. 11. Schematic temperature-entropy process path through compression, TES heat rejection, storage, TES reheat, and expansion. The entropy axis is qualitative; the companion exergy study reports absolute values and the turbine-exit state.

Table IV lists the validated anchor states this paper hands to that analysis.

Table Iv. Validated Thermodynamic State Points For The Exergy Bridge

Stage	**T (K)**	**Mass flow (kg/s)**	**Note**
Ambient inlet (dead state)	293	G_c = 0.247 (charge)	T_0 reference for ex
Compressor discharge	589	G_c = 0.247	Before TES intercooler

ISSN 2278-2540 | DOI: 10.51583/IJLTEMAS | Volume XV, Issue VII, July 2026

TES outlet / vessel charge	330	$G_c = 0.247$	After intercooler heat capture
TES reheat / turbine inlet	420	$G_b = 0.276$	T_{fa}, Section III.F

These four anchor temperatures, together with the validated power and mass-flow parameters W_c = 132.7 kW, P_t = 90 kW, β = 69.1, G_c = 0.247 kg/s, and G_b = 0.276 kg/s carried forward from Section III.F, are the same inputs used identically in the companion exergy analysis, which locates the residual gap between this paper's 67.8% RTE and an ideal reversible cycle physically, rather than leaving it as the single undifferentiated 32.2-percentage-point quantity this paper reports. That analysis identifies the compression and expansion trains, rather than the TES heat exchanger, as the dominant exergy-destruction nodes at this operating point, a finding this paper's dynamic results are consistent with: Section IV.D shows the turbine and compressor optimizations contributing more of the round-trip-efficiency gain, 7.2 and 6.4 percentage points, than the TES effectiveness improvement's 5.2 points.

B. Techno-Economic Foundation

The same validated operating point defines the technical boundary conditions for the companion techno-economic assessment. The system is sized around a rated discharge power P_t = 90 kW drawn against an installed PV capacity of 225 kWp, dispatched over top = 1,400 h/yr of peak-tariff hours to deliver an annual energy output of

$$E_{a0} = P_t \cdot t_{top} = 90 \cdot 1400 = 126000\ \mathrm{kWh/yr}\ (24)$$

Capital expenditure for the full 90 kW hybrid system totals USD 100,000, a figure the companion study documents in detail by component, and which reflects a firm, vendor-requoted estimate following a shift from underground cavern to modular above-ground pressure-vessel storage rather than the substantially higher parametric estimate an earlier costing pass had used before that re-quotation. Table V summarizes the boundary conditions this paper hands to that analysis.

Table V. Technical Boundary Conditions For The Techno-Economic Bridge

Parameter	**Value**	**Unit**
Rated discharge power, P_t	90	kW
PV installed capacity	225	kWp
Compression power, W_c	132.7	kW
Round-trip efficiency, RTE	67.8	Percent
Annual peak-dispatch hours, top	1,400	h/yr
Annual energy delivered	126,000	kWh/yr
Capital expenditure, CAPEX	100,000	USD
Project lifetime	25	Years

With these boundary conditions fixed, the companion study converts them into a Levelized cost of electricity through the standard annuity form [24],

$$LCOE = \frac{(CAPEX \cdot CRF + OPEX)}{E_{a0}}, CRF = r(1+r)^{\frac{N}{[(1+r)^{N-1}]}} (25)$$

ISSN 2278-2540 | DOI: 10.51583/IJLTEMAS | Volume XV, Issue VII, July 2026

and carries that figure through to a project-level net present value, internal rate of return, and payback period for the CUT Farm installation, using the SAPP peak and valley tariff structure as the revenue and charging-cost basis [24]. This paper does not re-derive those financial results; it fixes the technical inputs, P_t, W_c, RTE, and the annual dispatch profile, that make them possible.

CONCLUSIONS AND FUTURE RESEARCH

A multi-domain MATLAB/Simscape model of a 90 kW Solar PV Adiabatic CAES hybrid system for the CUT Farm has been built and exercised across a full charge and discharge cycle. The PV array and its incremental-conductance MPPT controller settle to a stable operating point within milliseconds, the Field-Oriented Control loops governing both the machine-side and grid-side converters damp cleanly after start-up against the d-q state equations of Section III.C, the two-stage compression train charges the storage vessel to its validated design pressure over a six-hour window while transferring the bulk of its compression heat into thermal storage, and the discharge train returns that heat to a radial inflow turbine to deliver a steady 90 kW with well-behaved current and torque dynamics.

Coordinated improvements to compressor, turbine, and TES performance raise the simulated round-trip efficiency from a 49.0% diabatic baseline to 67.8%, a result that sits comfortably above both operating CAES plants in the literature and the PV-CAES hybrid benchmark, and just under the theoretical ceiling reported for adiabatic architectures generally. A propagated uncertainty analysis shows that the performance of the physical prototype is expected to be in a 61.0 to 67.8% range, which is well above the diabatic floor at the high end of the range. The peak vessel pressure and TES temperature reported in Section IV are results of this specific six-hour simulated window, not the design-basis exergy and techno-economic values (β_{total} = 69.1, T_{fa} = 420 K) carried forward from Section V, which describe the discharge-side reheat design point rather than the charging-side TES thermal mass.

The two companion studies are founded on this validated dynamic and thermodynamic operating point: W_c = 132.7 kW, P_t = 90 kW, β = 69.1 and RTE = 67.8%. A companion exergy and entropy generation analysis applies second-law methods to the same validated operating point, using the state points of Section V.A, to locate, component by component, where within the compression train, the expansion train, and the TES heat exchange the residual 32.2 percentage point gap between this study's RTE and an ideal cycle actually resides, rather than leaving it as a single undifferentiated loss. Future work on this foundational model itself centers on replacing the idealized, perfectly sealed vessel and smooth irradiance ramps of Section IV.E with measured leakage and cloud-transient data from the physical prototype now under fabrication, and on resolving the schematic temperature-entropy trajectory of Section V.A into a fully stage-resolved path once per-stage Simscape export is available. Together, the three studies carry the CUT Farm Solar PV-A-CAES system from a validated dynamic model through to a fully characterized, economically and thermodynamically justified storage pathway for reliability-constrained agricultural sites across the Southern African Power Pool.

REFERENCES

1. E. F. Chipango, "Energy poverty in Zimbabwe," Energy Research & Social Science, vol. 75, p. 102026, 2021.
2. International Energy Agency (IEA), Africa Energy Outlook 2022, IEA, Paris, France, 2022.
3. X. Luo, J. Wang, M. Dooner, and J. Clarke, "Overview of current development in electrical energy storage technologies and the application potential in power system operation," Applied Energy, vol. 137, pp. 511 to 536, 2015.
4. S. Succar and R. H. Williams, "Compressed Air Energy Storage: Theory, Resources, and Applications for Wind Power," Princeton Environmental Institute Report, Princeton Univ., Princeton, NJ, USA, Apr. 2008.
5. M. Budt, D. Wolf, R. Span, and J. Yan, "A review on compressed air energy storage: Basic principles, past milestones and recent developments," Applied Energy, vol. 170, pp. 250 to 268, 2016.
6. F. Crotogino, K.-U. Mohmeyer, and R. Scharf, "Huntorf CAES: More than 20 years of successful operation," in Proc. Solution Mining Res. Inst. Spring Meeting, Orlando, FL, USA, 2001.

ISSN 2278-2540 | DOI: 10.51583/IJLTEMAS | Volume XV, Issue VII, July 2026

7. D. Wolf and M. Budt, "LTA-CAES: A low-temperature approach to adiabatic compressed air energy storage," Applied Energy, vol. 125, pp. 158 to 164, 2014.
8. H. Lund and G. Salgi, "The role of compressed air energy storage (CAES) in future sustainable energy systems," Energy Conversion and Management, vol. 50, no. 5, pp. 1172 to 1179, 2009.
9. W. He and J. Wang, "Optimal selection of air expansion machine in compressed air energy storage: A review," Renewable and Sustainable Energy Reviews, vol. 87, pp. 77 to 95, 2018.
10. Y. Kim, J. Lee, S. Kim, and D. Favrat, "Potential and evolution of compressed air energy storage: energy and exergy analyses," Entropy, vol. 14, no. 8, pp. 1501 to 1521, 2012.
11. R. Wang, W. Shi, X. Xue, C. Cao, K. Xue, and G. Xu, "Performance analyses of a novel compressed air energy storage system integrated with the solar power plant," SSRN preprint, 2025.
12. L. Geissbuhler, V. Becattini, G. Zanganeh, S. Zavattoni, M. Barbato, A. Haselbacher, et al., "Pilot-scale demonstration of advanced adiabatic compressed air energy storage, Part 1: plant description and tests with sensible thermal-energy storage," Journal of Energy Storage, vol. 17, pp. 129 to 139, 2018.
13. X. Luo, J. Wang, C. Krupke, Y. Wang, Y. Sheng, J. Li, Y. Xu, D. Wang, S. Miao, and H. Chen, "Modelling study, efficiency analysis and optimisation of large-scale adiabatic compressed air energy storage systems with low-temperature thermal storage," Applied Energy, vol. 162, pp. 589 to 600, 2016.
14. Y. Zhang, K. Yang, X. Li, and J. Xu, "The thermodynamic effect of thermal energy storage on compressed air energy storage system," Renewable Energy, vol. 50, pp. 227 to 235, 2013.
15. E. Barbour, D. Mignard, Y. Ding, and Y. Li, "Adiabatic compressed air energy storage with packed bed thermal energy storage," Applied Energy, vol. 155, pp. 804 to 815, 2015.
16. Sciacovelli et al., "Dynamic simulation of adiabatic compressed air energy storage (A-CAES) plant for grid-scale applications," Applied Energy, vol. 154, pp. 690 to 705, 2015.
17. X. Luo, M. Dooner, W. He, J. Wang, Y. Li, D. Li, and O. Kiselychnyk, "Feasibility study of a simulation software tool development for dynamic modelling and transient control of adiabatic compressed air energy storage with its electrical power system applications," Applied Energy, vol. 228, pp. 1198 to 1219, 2018.
18. MathWorks, Simscape and Simscape Fluids Documentation, Release R2024b, The MathWorks, Inc., Natick, MA, USA, 2024.
19. Safari and S. Mekhilef, "Simulation and hardware implementation of incremental conductance MPPT with direct control method using Cuk converter," IEEE Transactions on Industrial Electronics, vol. 58, no. 4, pp. 1154 to 1161, 2011.
20. P. Pillay and R. Krishnan, "Modeling, simulation, and analysis of permanent-magnet motor drives, Part I: the permanent-magnet synchronous motor drive," IEEE Transactions on Industry Applications, vol. 25, no. 2, pp. 265 to 273, 1989.
21. J. Holtz, "Pulsewidth modulation for electronic power conversion," Proceedings of the IEEE, vol. 82, no. 8, pp. 1194 to 1214, 1994.
22. T. J. Kotas, The Exergy Method of Thermal Plant Analysis, Butterworths, London, UK, 1985.
23. International Renewable Energy Agency (IRENA), Renewable Power Generation Costs in 2023, IRENA, Abu Dhabi, UAE, 2024.
24. Zimbabwe Energy Regulatory Authority (ZERA), Approved Electricity Tariff Schedule, ZERA, Harare, Zimbabwe, 2024